ARTICLE

Lithium metal atoms fill vacancies in the germanium network of a type-I clathrate: Synthesis and structural characterization of $Ba_8Li_5Ge_{41}$

Received 00th January 20xx,
Accepted 00th January 20xx

DOI: 10.1039/x0xx00000x

Kowsik Ghosh[a], Alexander Ovchinnikov[a,b], Michael Baitinger[c], Mitja Krnel[c], Ulrich Burkhardt[c], Yuri Grin[c], and Svilen Bobev[a,*]

Clathrate phases with crystal structures exhibiting complex disorder have been the subject of many prior studies. Here we report syntheses, crystal and electronic structure, and chemical bonding analysis of a Li-substituted Ge-based clathrate phase with the refined chemical formula $Ba_8Li_{5.0(1)}Ge_{41.0}$, which is a rare example of ternary clathrate-I where alkali metal atoms substitute framework Ge atoms. Two different synthesis methods to grow single crystals of the new clathrate phase are presented, in addition to the classical approach towards polycrystalline materials by combining pure elements in desired stoichiometric ratios. Structure elucidations for samples from different batches were carried out by single-crystal and powder X-ray diffraction methods. The ternary $Ba_8Li_{5.0(1)}Ge_{41.0}$ phase crystallizes in the cubic type-I clathrate structure (space group $Pm\bar{3}n$ no. 223, $a \approx 10.80$ Å), with the unit cell being substantially larger compared to the binary phase Ba_8Ge_{43} ($Ba_8\square_3Ge_{43}$, $a \approx 10.63$ Å). The expansion of the unit cell is the result of the Li atoms filling vacancies and substituting atoms in the Ge framework, with Li and Ge co-occupying one crystallographic (6*c*) site. As such, the Li atoms are situated in four-fold coordination environment surrounded by equidistant Ge atoms. Analysis of chemical bonding applying the electron density/ electron localizability approach reveals ionic interaction of barium with the Li–Ge framework, while the lithium-germanium bonds are strongly polar covalent.

Introduction

Intermetallic clathrates [1,2] with their unique cage-like structures have received much research attention; the chemistry and physics communities have been pursuing various clathrates because of their superconducting [3–7], thermoelectric [8–15], and magnetic [16,17] properties. In recent years clathrates have also been investigated as potential electrode materials in Li-ion batteries. [18–22]

Among the several types of crystal structures for the clathrates, the structure of the type-I clathrates is represented by the largest number of compositions. There are two distinct cages in the framework of the type-I clathrates, which is typically made up of group 14 elements (tetrels, *Tt* = Si, Ge, Sn), as shown in **Figure 1**. The cages accommodate guest atoms, most commonly alkali or alkaline-earth metals. [2,23–25,26–29]. Guest atoms take the crystallographic 2*a* and 6*d* Wyckoff sites in the cubic space group $Pm\bar{3}n$. The guest atom at 2*a* is enclosed in a 20-atom cage (pentagonal dodecahedron, Tt_{20}), and that at 6*d* in a 24-atom cage (tetrakaidecahedron, Tt_{24}), respectively. The Tt_{20} cage has 12 pentagonal faces, while the larger Tt_{24} cage has 12 pentagonal and 2 hexagonal faces (**Figure 1b**).

Framework-building Si, Ge, and Sn atoms can be partially substituted by group 13 elements (Al, Ga, In) [3,8,9,11,30–34] and some late transition metals (e.g., Cu, Ni, or noble metals) [35–39]. In addition to the said chemical substitutions, physical properties of clathrates also depend on the defects (vacancies) that can form on framework sites, where the amount and the ordered/disordered distribution of the defects in the framework become of particular importance. [35,40] Defects and chemical substitutions can also occur on the guest atom sites, allowing for enhanced tunability of compositions and properties. These ideas have been extensively exploited in the context of the "phonon-glass electron-crystal" concept, and speculated to allow for a semi-independent control over heat- and charge- transport properties in these materials. [13,14,39]

Studies of Ba/Ge-based clathrates have been widely pursued with many prior reports available in the literature.[3,10,15, 16,25,32,33,36,39,41,42–47] The parent type-I clathrate is known to host defects on the Ge framework and its formula is denoted as $Ba_8\square_3Ge_{43}$ (□ stands for framework vacancies) [28,46]. The clathrate-I framework consists of three crystallographically independent germanium atoms, labelled as Ge1, Ge2 and Ge3, situated at positions 6*c*, 16*i* and 24*k*,

[a] *Department of Chemistry and Biochemistry, University of Delaware, Newark, Delaware 19716, United States.*
[b] *Faculty of Chemistry and Food Chemistry, Technische Universität Dresden, 01062 Dresden, Germany.*
[c] *Max Plank Institut für Chemische Physik fester Stoffe, 01187 Dresden, Germany.*

* Corresponding author Email: bobev@udel.edu.
Electronic Supplementary Information (ESI) available: tables with crystallographic data for all refined structures; results from scanning electron microscopy work; results from electrical resistivity. See DOI: 10.1039/x0xx00000x

respectively, (**Figure 1b**). In the idealized case of Ba_8Ge_{46}, with a total of 46 Ge atoms per unit cell, there are no vacant Ge sites. In the structure of the actual phase that forms, approx. 3 of the 46 Ge atoms are missing. The vacancy arrangement has been described in two principal ways: i) first, in a disordered fashion; ii) second, by modelling of the vacancies in the framework in an ordered fashion. In the former, classical type-I structural description (space group $Pm\bar{3}n$), the three defects occur at the 6*c* sites only. This means the Ge1 site occupation factor is close to 50%.[28] In the latter case, ordering can be achieved in the space group $Ia\bar{3}d$, effectively creating a 2×2×2 superstructure.[48] The fully crystallographically-ordered version of the $Ba_8Ge_{43}\square_3$ structure, however, does not always materialize, as exemplified by the crystals obtained via other methods available for the synthesis.[33] Another peculiarity concerning the ordering of defects in Ge-clathrates can be inferred from the studies on K-Li-Ge samples—as shown for example for the specimen $K_8Li_{2.29(16)}Ge_{43.47(3)}\square_{0.24(15)}$, a prolonged annealing at 673 K is required before signs of superstructure reflections can be observed.[49]

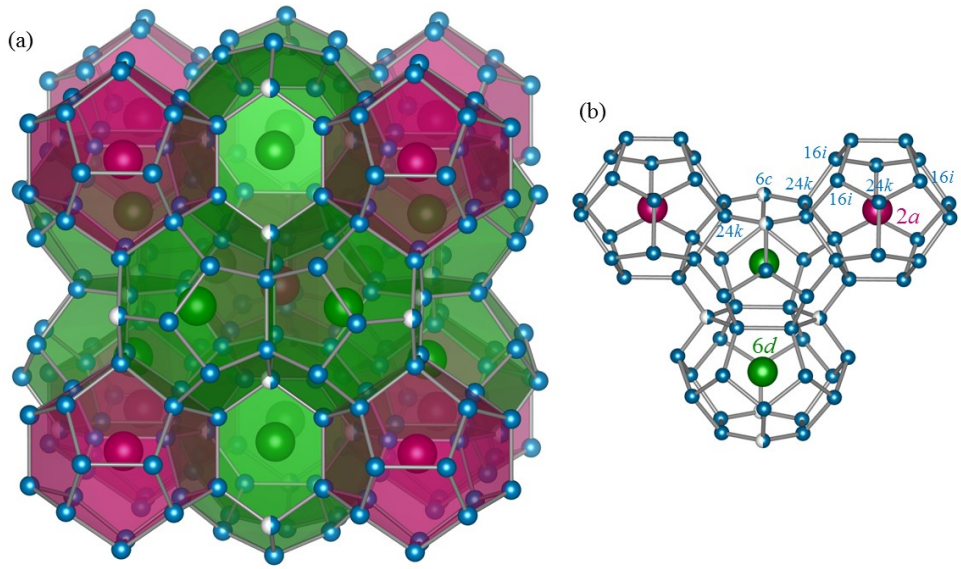

Figure 1. (a) Representation of the cubic crystal structure of the type-I clathrates (space group $Pm\bar{3}n$) in polyhedral mode. (b) Close up view showing the interconnection of the polyhedra with the crystallographic sites labelled. If the structure is to be interpreted as $Ba_8Ge_{43}\square_3$, magenta and green colors represent the Ge_{20} and Ge_{24} cages occupied by Ba1 and Ba2, respectively. Ge vacancies are located on site 6*c* only (ca. 50%, randomly distributed). Ge atoms are drawn as blue spheres. For the structure of the title $Ba_8Li_5Ge_{41}$ clathrate, the site 6*c* is co-occupied by Li and Ge in a ratio of approx. 5:1.

Given the propensity of the Ba/Ge-based clathrates to accommodate a sizeable number of Ge-vacancies, one can appreciate the difficulties that would be encountered when a third chemical element is introduced into the framework, "converting" the binary phase to a ternary one. For instance, type-I clathrates with nominal compositions $Ba_8T_xGe_{46-x}$ (*T* = Ga, Zn, Cd, Ni, Pd, Pt, Cu, Ag, and Au) have been studied and reported by us and by various groups [13,25,30,31,32,36,37,46–49,52]. In many of the latter cases, substitutions and vacancies coexist; the recent comprehensive investigation in the Ba-Au-Ge system is a testament to the level of complexity.[52]

In contrast to the frequent studies on the substitution patterns with transition metal elements, clathrates containing Li remain under-explored [63]. The scarcity of the experimental data can be explained by the fact that the size of the Li atom makes it an unfavorable choice for a guest atom for incorporation into the large polyhedral cages [53]. This particularly holds true for Ge- and Sn-based clathrate-I phases, which are not reported even with the larger Na atoms [53]. Recently, from synchrotron data, Dopilka *et al.* suggested that the lithiation pathways into the $Ba_8Ge_{43}\square_3$ structure,[54] involve lithium atoms filling framework vacancies, which ultimately lead to amorphization of the clathrate and the formation of Li_7Ge_{12}, $BaGe_2$ and Li_7Ge_3 after full lithiation. Density functional theory calculations also show that lithiation in $Ba_8Ge_{43}\square_3$ is energetically favorable by the said mechanism [33], yet, no experimental details concerning the possible existence of a ternary Ba-Li-Ge clathrate are available to date. However, there already exist a precedent for Li and Ge atoms to share a framework site in clathrate-I, demonstrated by Liang *et al* for the Li-substituted ternary clathrate-I $K_8Li_xGe_{44-x/4}\square_{2-3x/4}$ ($0 < x < 2.67$).[49,53] Therefore, we embarked on a systematic structural investigation of the speculated Ba-Li-Ge clathrate phase. In this contribution, we report the synthesis and the structural characterization of the first structurally characterized clathrate type-I involving the three respective elements. The chemical formula of this new ternary compound is best represented as $Ba_8Li_xGe_{42-x/4}\square_{4-3x/4}$ ($0 < x < 5.33$), although for brevity, hereafter we will refer to it as $Ba_8Li_5Ge_{41}$.

Experimental

Synthetic procedures

In the past, single crystals of clathrates were grown from sub-liquidus region of the according phase diagrams either employing Czochralski technique, e.g. Ref. 64, or using elements with low melting points as fluxes, for example Ga for $Eu_8Ga_{16}Ge_{30}$ [34]. In this paper, we introduce processes involving Pb-flux and LiCl-flux to grow single crystals of $Ba_8Li_5Ge_{41}$. Three different types of synthesis are referred to as method *A*, *B*, and *C* hereafter. The starting elements, Ba, Li, Ge, and Pb were purchased from Sigma-Aldrich and Alfa Aesar with stated purity ≥ 99.9 wt. % and were used without further purification (Li surface was cleaned with a scalpel blade immediately before use). Lithium chloride, LiCl (anhydrous, Alfa Aesar, ≥ 99.9 wt. %), was additionally dried under dynamic vacuum at 823 K for 30 min before transferring into an argon-filled glovebox in a sealed container. All materials were weighed in the desired stoichiometric ratios inside the glovebox.

Methods *A* and *B* made use of Pb as a flux. Different types of crucibles were employed, made of alumina and niobium, respectively, and the grown crystals were investigated by single-crystal X-ray diffraction. These experiments were pursued in order to rule out potential sample- contamination from crucible material. For synthesis method *C*, molten LiCl was utilized as a flux (and potential source of extra Li). In all cases, the crucibles were transferred out of the glovebox in fused silica tubes, which were subsequently evacuated and flame-sealed. For methods *A* and *B* there was a single high-temperature step; experiments *C* were carried out in two steps. The details will be discussed in the next section.

Caution! *Lead and lead-containing materials are hazardous and the reaction temperature is sufficiently high to sustain high vapor pressure of lead. Additionally, care needs to be exercised since lithium can cause the breakage of the alumina crucible at high temperature and molten Li can reduce the silica tube. Therefore, all described experimental procedures have to be performed in the well-ventilated environments by using additional precautions, such as personal protective equipment in case of the potential failure of the silica tubes. Use of thick (1.5+ mm) silica tubes is mandatory.*

Crystallography

Powder X-ray diffraction. Powder X-ray diffraction (PXRD) measurements were carried out at room temperature on a Rigaku Miniflex diffractometer (filtered Cu Kα radiation, λ = 1.5418 Å), operated inside a nitrogen-filled glovebox. Small portions of the obtained single crystals were ground into powder using agate mortars and pestles. The data were collected between 5 and 75° in 2θ with a step size of 0.05° and 2 s per step counting time. The PXRD measurements before and after exposure to air over a long period of up to six weeks have been taken to confirm the stability of the phase in air (**Figure S1** in the supporting information section). For the final determination of lattice parameter, PXRD measurements were also done using a Guinier camera (Cu Kα1 radiation, λ = 1.54056 Å). The reflection positions were individually determined by profile fitting and corrected with LaB_6 standard (NIST, a = 4.15692(1) Å). Room temperature unit cell parameter for the sample obtained via method *A*, refined from the corresponding Guinier powder pattern with LaB_6 as an internal standard, was 10.8128(2) Å.

Single-crystal X-ray diffraction. Suitable single-crystals were selected and were cut under dry Paratone-N oil to appropriate dimensions ($d \leq 0.10$ mm). After that, crystals were scooped by MiTeGen plastic loops and transferred to the goniometer of a Bruker APEX II diffractometer, equipped with monochromatized Mo Kα radiation, λ = 0.71073 Å. The experiments were done at T = 200(2) K, maintained by a stream of cold nitrogen gas. Data sets were processed with the SAINT and SADABS software packages. Refinement by full-matrix least-squares minimizations were carried out with either SHELXL [55,56] on F^2 or WinCSD [57] on F. Atomic coordinates and labels were set to be consistent with previous studies [7].

Selected details of the data collection and relevant crystallographic parameters of the samples from *A*, *B* and *C* methods are given in **Table 1** and **Table S1-S6**, respectively (*supplementary information*). CCDC 2257289-2257292 contain the full supplementary crystallographic data. The CIF can be obtained free of charge via www.ccdc.cam.ac.uk/data_request/cif, or by emailing data_request@ccdc.cam.ac.uk, or by contacting The Cambridge Crystallographic Data Centre, 12 Union Road, Cambridge CB2 1EZ, U.K., fax +44 1223 336033

Table 1. Crystallographic information for $Ba_8Li_5Ge_{41}$, synthesized by *A* method.

Empirical formula	$Ba_8Li_{5.0(1)}Ge_{41.0}$
Formula weight (g mol^{-1})	4109.69
Temperature (K)	200
Radiation (λ)	Mo $K\alpha$, 0.71073 Å
Crystal system	Cubic
Space group, Z	$Pm\bar{3}n$ (No. 223), 1
a (Å)[a]	10.8128(2)
V (Å^3)	1264.20(7)
ρ_{calc} (g cm^{-3})	5.41
μ (cm^{-1})	316.5
Goodness-of-fit on F^2	1.02
R_1 ($I \geq 2\sigma_I$)[b]	0.0346
wR_2 ($I \geq 2\sigma_I$)[b]	0.0381
CCSD number	2257289

[a] From the standardized X-ray powder diffraction data

[b] $R_1 = \sum||F_o|-|F_c||/\sum|F_o|$; $wR_2 = [\sum[w(F_o^2-F_c^2)^2]/\sum[w(F_o^2)^2]]^{1/2}$, where $w = 0.8903\log(F_o)^4$.

X-ray energy-dispersive (EDX) analysis

Single crystals were selected and mounted on a carbon tape, glued to an aluminum holder. The analyses were performed on Auriga 60 Cross Beam Scanning Electron Microscope equipped with Oxford Synergy X-MAX80 & EBSD (electron backscattering diffraction) X-ray energy-dispersive (EDX) spectrometer. The beam current was 10 µA at 20 kV accelerating potential. Data were collected over several spots and averaged. A

representative image and elemental analysis are shown in **Figure S2**.

X-ray wavelength-dispersive (WDX) analysis

The chemical composition of selected crystals has been determined by WDX analysis (wavelength dispersive X-ray) on Cameca microprobe (SX 100, tungsten cathode). Several crystals with dimensions of approx. 100 µm were mounted in electrically conductive resin and metallographically polished with diamond finishing (**Figure 2** and **Figure S3**). WDX measurements have been performed with an electron beam of 20 kV / 15 nA of the acceleration voltage and the beam current, respectively. The intensities of the X-ray lines Ba Lα and Ge Kα measured on the crystals were compared with the respective intensities of the reference material Ba_6Ge_{25}. The ZAF matrix correction methods were applied to calculate mass concentrations of Ba and Ge. The given element amounts and statistical errors result from averaging on 10 measuring points.

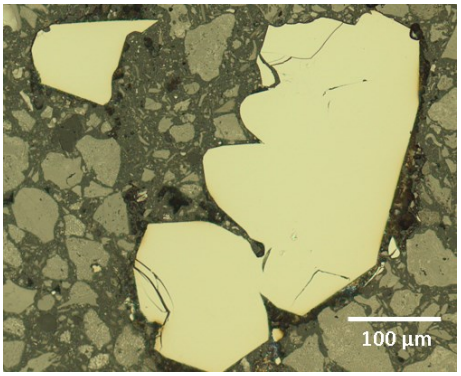

Figure 2. Optical microscopy image of cut and polished crystals of $Ba_8Li_5Ge_{41}$ grown by method A. The same specimens were further investigated by SEM/WDXS, yielding an averaged Ba:Ge = 1:5.1.

Electrical resistivity measurements

The electrical resistivity ρ was measured on a mm-sized single crystalline sample by using Quantum Design Physical Properties Measurement System (PPMS). AC electrical resistivity $\rho(T)$ was measured at fixed temperatures between T = 2 and 300 K in $\mu_0 H$ = 0 and 9 T magnetic field by applying I = 0.01 mA current pulse with frequency ω = 93 Hz for t = 1 s. The resistivity was measured by using the standard four-terminal technique.

Electronic structure calculations

The quantum chemical calculations were performed employing the all-electron, full-potential local orbital method (FPLO) within the local density approximation [65] and the Perdew-Wang parametrization.[66] Experimentally obtained lattice parameter and atomic coordinates were employed for the calculations on the ordered model of $Ba_8Li_5Ge_{41}$ in the space group $P1$. The electron localizability approach was used for the analysis of the chemical bonding in position space [67,68,79]. For this purpose, the electron localizability indicator (ELI) in its ELI-D representation [69] and the electron density (ED) were calculated with a specialized module in the FPLO code [70]. The topologies of ELI-D and ED were evaluated by means of the program DGrid.[71] The atomic charges from ED and bond populations of bond basins from ELI-D were obtained by integrating the ED within the basins (space regions), bounded by zero-flux surfaces in the according gradient field. This procedure follows the Quantum Theory of Atoms in Molecules (QTAIM [72]). For the analysis of the polarity of bonds, the intersection of the atomic basins in ED with the bond basins in ELI-D was employed. [73,74,75]

Results and discussions

Notes on the synthesis and crystal growth conditions

The motivation to search for a ternary Ba-Li-Ge clathrate came from the earlier electrochemical lithiation studies of binary $Ba_8Ge_{43}\square_3$, which led to amorphization of the clathrate phase.[54] Since we were unsuccessful in the quest to produce suitable crystals of the targeted clathrate phase from experiments involving Ba, Li, and Ge in Nb ampoules, we chose to carry out flux synthesis. It must be mentioned, however, that a ternary clathrate phase exists at 973 K along the composition range $Ba_8Li_xGe_{42-x/4}\square_{4-3x/4}$ connecting the binary high-temperature phase $Ba_8Ge_{43}\square_3$ with the ternary composition $Ba_8Li_{5.33}Ge_{40.67}$. For the details on phase equilibria, the reader is referred to the paper by Liang *et al.* in a later issue of the journal.[76] The present study deals with crystal growth methods of this phase in order to enable a detailed investigation of the complex crystal structure for the compositions obtained.

For crystal growth experiment using Pb flux, the elements Ba:Li:Ge:Pb were weighed in the ratio of 3.5:14:14:68.5; the elemental mixtures were put in a alumina crucible (method A) and a Nb crucible (method B). The crucibles were topped with a piece of quartz wool and jacketed in evacuated fused silica tubes. Via trial and error, the optimized temperature profile was established for the *A* and *B* synthesis methods as follows: the evacuated sealed tubes with reaction mixture were heated to 473 K for 2 h, followed by heating at 623 K for 2 h and at 973 K for 10 h (with the heating rate of 50 K/h for all three steps). Then, the reaction mixtures were slowly cooled down to 823 K at a cooling rate of 3 K/h. The tubes were taken off from the furnace at this point, allowing the molten Pb metal to be separated from the solid product. The process was completed in less than 30 seconds, using a standard centrifuge, by flipping the tubes and spinning the rotor at high speeds (ca. 3-4000 rpm). $Ba_8Li_5Ge_{41}$ with the clathrate type-I structure was the main product from both synthesis routes under the stated conditions. When the amount of Li in the starting composition is reduced, the clathrate still forms, but the yields decrease. For instance, when a reaction was carried out with Ba, Li, Ge and Pb in molar ratio of 1:2:4:20, following method *A*, only a small number of $Ba_8Li_5Ge_{41}$ crystals were

found, alongside crystals of recrystallized elemental Ge. Crystallographic data for this work are provided as supplementary material (**Table S3** and **Table S6**). Structure refinements for crystals grown via methods *A* and *B* are very much alike (**Table 1** and **Table S1**), with their major structural metrics being virtually indistinguishable (e.g. refined compositions are identical within the margin of error). This is suggestive that inadvertent incorporation of container material into the clathrate structure is unlikely. A two-step procedure was employed in method *C*. In the first step, the elements Ba, Li and Ge were weighed in the molar ratio of 1:4:8 inside the glovebox. The elements were loaded into a niobium tube, which was sealed under 600 mbar of high-purity argon gas using a home-built arc-welding apparatus. The Nb tube was then placed inside an evacuated fused silica tube, which was subsequently flame-sealed. The tube was heated to 1023 K with a rate of 200 K/h, kept at this temperature for 48 h and cooled down to room temperature with a rate of 5 K/h. Approximately 0.25 g of the multi-phase solid product from the first step was mixed with 0.15 g of dry LiCl in an alumina crucible, topped with a piece of quartz wool. The rest of the procedure was similar to that used in methods B and C, except that the centrifugation was carried out at a temperature of 923 K (i.e., above the melting point of LiCl, $T_m \approx 878$ K).

The described procedure produced sub-millimeter-sized crystals of $Ba_8Li_5Ge_{41}$ and another, yet unidentified phase. By comparison, the experiments with Pb-flux afforded much bigger crystals, some as large as 1-2 mm in all dimensions (**Figure 2 and Figure S2**).

Crystal structure

The incorporation of Li atoms into the clathrate structure was studied by single-crystal X-ray diffraction methods. Below, we will focus on the structural subtleties that helped establish the structure as $Ba_8Li_x\square_{4-3x/4}Ge_{42-x/4}$ ($x \approx 5.0$-5.1) and differentiate the latter model from the other two possibilities, namely $Ba_{8-y}Li_y\square_xGe_{46-x}$ and $Ba_8\square_xGe_{46-x}$.

The most conclusive evidence for incorporation of Li atoms into the clathrate structure comes directly from the single-crystal work. The robustness of the $Ba_8Li_x\square_{4-3x/4}Ge_{42-x/4}$ structural model can be readily tested against a hypothetical lithium-free model with the same space group $Pm\bar{3}n$ (the basic crystal structure was already described in the Introduction and a structural representation was given in **Figure 1**). In this case, the reduced electron density on site 6*c* (Ge1) can be modelled as simple under-occupation, which results in an occupancy factor of about 21%, while the occupation factors of the sites 16*i* (Ge2) and 24*k* (Ge3) do not deviate from 100 %. Likewise, Ba1 and Ba2 atoms in the crystallographic sites 2*a* and 6*d*, respectively, were found to be fully occupied (Ba2 has an enlarged anisotropic displacement parameter, which is more consistent with the notion of positional, not occupational disorder, as shown later in the paper). This leads to a refined formula $Ba_8\square_{4.7}Ge_{41.3}$. Importantly, the characteristic elongated thermal ellipsoids of the Ge3 atoms, that are immediate neighbors of the vacancies, coupled with the unphysical distances as observed in $Ba_8\square_{3.2}Ge_{42.8}$[33], are not present here (**Figure 3**).

Additional experimental evidence lending support to the formulation $Ba_8Li_x\square_{4-3x/4}Ge_{42-x/4}$ also comes from basic crystallographic data. As seen from **Table 1** and the tables in supporting information, the unit cell parameters from all synthesized samples are $a \approx 10.80$ Å—much larger than the parameter of the binary $Ba_8\square_3Ge_{43}$ (a = 10.6565(2) Å)[28] and $Ba_8\square_{3.2}Ge_{42.8}$ clathrates (a = 10.6335(15) Å).[33] The observed larger unit cell volumes, together with the electron densities calculated from the single-crystal X-ray diffraction data, unequivocally support the idea that the Li atoms do *not* substitute Ba atoms in the structure. Since the atomic radius of the barium atom ($r_{Ba} \approx 2.17$ Å) [59] is larger than that of the lithium atom ($r_{Li} \approx 1.52$ Å) [59], if the products of the Ba-Li-Ge reactions were $Ba_{8-y}Li_y\square_xGe_{46-x}$, a small volume contraction of the unit cell parameter of the ternary compared to the binary clathrates would be expected [60]. In this context, an expanded unit cell compared to binary $Ba_8\square_3Ge_{43}$, despite the lower electron density at position 6*c* can only be explained with the substitution of germanium by lithium. These facts, combined with the observations made previously for the analogous $K_8Li_xGe_{44-x/4}\square_{2-3x/4}$ clathrates [53], bolster the notion for the existence of ternary Ba-Li-Ge clathrates and the proposed role of the Li atoms as filling crystallographic positions nominally taken by Ge in the binary representative.

Another parallel can be drawn between the structures of the binary clathrate $K_8\square_2Ge_{44}$ (a = 10.686(4) Å) [27] and its ternary variant $K_8Li_{2.67}Ge_{43.33}$ (a = 10.7702(1) Å) [53]. Here too, an expansion of the unit cell is observed because the Li atoms get incorporated in the framework rather than in the guest sub-structure. One should also notice that $Ba_8\square_3Ge_{43}$ with three framework vacancies per formula unit has a *smaller* unit cell volume compared to $K_8\square_2Ge_{44}$ with just two framework vacancies per formula. At the same time, $Ba_8Li_5Ge_{41}$ has a *larger* unit cell volume compared to $K_8Li_{2.67}Ge_{43.33}$. This is the case because the former structure has a higher Li content compared to the latter one. We can also compare single-crystal data of a similar type-I clathrate, $K_8Cd_{3.77(7)}Ge_{42.23}$ [60], with a larger unit cell parameter (a = 10.8710(4) Å) compared to both $Ba_8Li_5Ge_{41}$ and $K_8Li_{2.67}Ge_{43.33}$, with the reason being the larger atomic radius of Cd compared to Li. Another comparison can be made to the Ba/Ge-clathrates $Ba_8Pd_3Ge_{43}$ (a = 10.756 Å) [43], $Ba_8Ga_{16}Ge_{30}$ (a = 10.793 Å) [25] and $Ba_8Zn_8Ge_{38}$ (a = 10.758 Å) [44] —their structures are all characterized based on single-crystal data refinements and are indicated to be devoid of framework vacancies—note that the given unit cell parameters are close to that of $Ba_8Li_5Ge_{41}$.

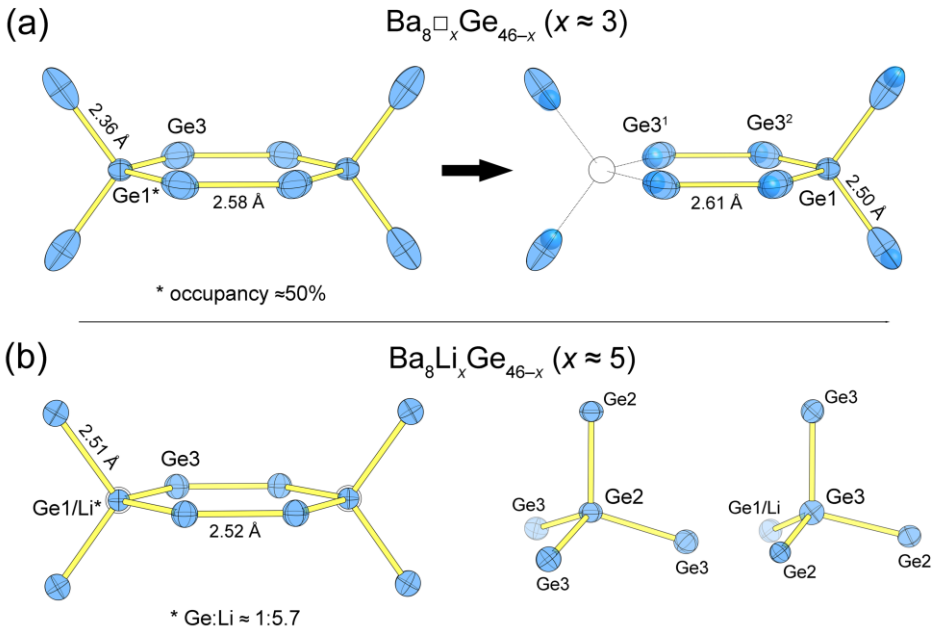

Figure 3. (a) Schematic representation of the section of the $Ba_8\square_xGe_{46-x}$ ($x \approx 3$) structure, where the Ge vacancies occur (on site 6*c* only, Ge1). The local distortion of the framework when a Ge atom is missing is modelled by splitting Ge3 into Ge3¹ and Ge3², which alleviates the issue with the unphysical average Ge1–Ge3 distance, (b) Schematic representation of the section of the $Ba_8Li_x\square_{4-3x/4}Ge_{42-x/4}$ ($x \approx 5.0$–5.1) structure where Li/Ge disorder is prevalent. For comparison, the local coordination of Ge2 and Ge3 atoms are also shown. All relevant distances are tabulated in Table 3. Thermal ellipsoids are drawn at the 90% probability level.

If one considers all of the above, the incorporation of Li atoms and their placement within the clathrate structure can be argued as unequivocally established. However, the amount of Li present in the samples remains an open question. Taking into account the previously discussed model refined as $Ba_8\square_{4.7}Ge_{41.3}$, it is apparent that almost 5 Ge atoms are missing or substituted by Li atoms. Being that the limiting number of vacancies per the Zintl concept,[61] in a binary Ba-Ge clathrate is 4, i.e., $Ba_8\square_4Ge_{42}$, such high concentration of vacancies can be deemed improbable, leaving the second hypothesis, namely, that ca. 5 Ge atoms per formula unit are substituted by Li atoms as more likely. The final refined composition of $Ba_8Li_{\sim 5}Ge_{\sim 41}$ (**Table 1**) is in an excellent agreement with elemental analysis results. Though the light lithium was not detectable by the X-ray energy dispersive (EDX) or wavelength dispersive (WDX) spectrometers, the observed atomic ratio of Ba:Ge (1:5.17; **Figure 2**) is very close to the calculated ratio from the single crystal work (1:5.13).

On this note, we will also recall that X-ray diffraction methods cannot distinguish between underoccupation and mixed Li/Ge occupation in the framework sites with observed reduced electron density. Therefore, there remains the possibility that not all vacancies are filled with Li, and the actual composition of the phase is described by the formula $Ba_8Li_x\square_{4-3x/4}$ $Ge_{42-x/4}$ ($0 \le x \le 5.33$). At present, we can only ascertain that the occupation factors of Li/Ge on the 6*c* sites in all synthesized crystals were in the narrow range Li (84–86 at%) and Ge (16–14 at%), indicating that under flux-growth conditions, the crystals preferentially form with a composition near the limiting one, as deduced from the Zintl concept. There could be some defects present, but from the detailed analysis of the atomic displacement parameters (**Figure 3**) and bond lengths (*vide infra*), one can infer that their concentration is very low, not more than 0.1 per formula unit.

More details on the structural refinements for $Ba_8Li_xGe_{42-x/4}\square_{4-3x/4}$ ($x \approx 5.0$-5.1) follow. In an agreement with the model for $K_8Li_xGe_{44-x/4}\square_{2-3x/4}$, [53] where Li atom is sharing the 6*c* sites with Ge1 atom, we also only find Li/Ge1 disorder. The final residual values (R_1 = 0.0346 and wR_2 = 0.0381) from **Table 1** indicate the excellent fit to the experimental data. The refinements that were carried out for the samples synthesized via *B* and *C* methods also gave excellent refinement statistics (**Tables S1-S2**). Refined atomic coordinates are tabulated in **Table 2** and **Tables S4-S6** for products synthesized by *A*, *B* and *C* methods, respectively.

Table 2. Atomic coordinates and equivalent isotropic displacement parameters (B_{eq}[a] in Å²) for $Ba_8Li_5Ge_{41}$ synthesized by *A* method.

atom	site	*x*	*y*	*z*	B_{eq}
Ba1	2*a*	0	0	0	0.75(2)
Ba2 [b]	48*l*	0.0146(4)	0.5151(4)	0.2377(2)	0.8(3)
Li/Ge1 [c]	6*c*	1/4	1/2	0	0.9(7)
Ge2	16*i*	0.18304(7)	*x*	*x*	0.85(1)
Ge3	24*k*	0.1160(1)	0.3097(1)	0	1.00(2)

[a] B_{eq} is defined as one third of the trace of the orthogonalized B_{ij} tensor. The anisotropic displacement factor exponent takes the form: $-2\pi^2[(ha^*)^2B_{11} + \ldots + hka^*b^*B_{12}]$.
[b] The 6*d* position (0 ½ ¼) where Ba2 normally resides was 8-fold split. As a result, Ba2 at 48*l* is 1/8 occupied.
[c] Refined occupation factor: Li/Ge1 = 0.835(8)Li + 0.165Ge.

Close views of sections of the structure where Li/Ge disorder is prevalent are provided in **Figure 3**. The lithium atoms are located in two opposite corners of the hexagonal faces of the tetrakaidecahedral cage (site 6*c*). The presence of Li atoms at any other sites can be ruled out because the corresponding site occupation factors refined freely to within 3-4σ from 100%. The Li atoms are surrounded by four Ge3 atoms only (**Figure 3**). The angles within the Li-tetrahedra (four equidistant Ge3 atoms) are 109.4° and 109.7° and are very close to the ideal tetrahedral angle of 109.5°. Similarly, bond angles around the Ge2 atom deviate slightly from the tetrahedral, but the average is still close to the ideal value since Ge2 always has four bonds to neighboring atoms. The most significant deviation from the ideal tetrahedral angle is observed in the Ge3 coordination environment, with Li/Ge1-Ge3-Ge3 = 125.1°.

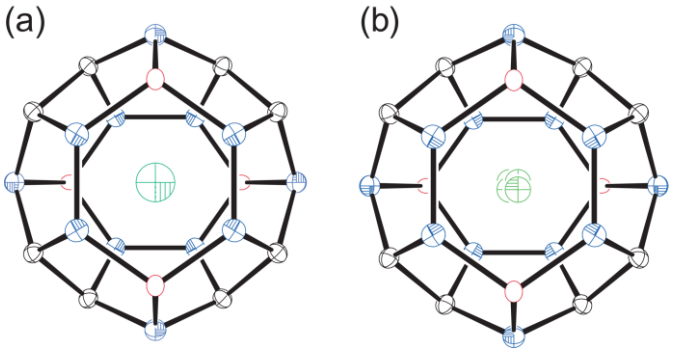

Figure 4. (a) Representation of the tetrakaidecahedral cage within the $Ba_8Li_5Ge_{41}$ structure, where Ba2 is at the center 6*d* position (0 ½ ¼). (b) Representation of the tetrakaidecahedral cage within the $Ba_8Li_5Ge_{41}$ structure, where Ba2 is off-centered at 48*l* position (0.02 0.51 0.24). Thermal ellipsoids are drawn at the 90% probability level. Ge1/Li on site 6*c* is represented with an ellipsoid shown in red and with outlines, Ge2 on site 16*i* is represented with a black ellipsoid with principal ellipses, Ge3 on site 24*k* is represented with a blue ellipsoid with octant shading.

There are no enlarged/elongated thermal ellipsoids refined for any of the Ge atoms. A possible anomaly may be inferred from the comparatively large B_{eq} for Ba2 (**Figure 4**, **Tables S4-S6**). Inspection of the anisotropic displacement parameter shows that its mean-principal directions are as follows: B_{11} = B_{22} > B_{33}. Precedents for such behavior of the atom filling the larger Ge_{24} cage exist and are well-documented in the literature on type-I clathrates; often times the elongated thermal ellipsoid is ascribed to a "rattling" motion. Such dynamic disorder may shift the Ba atoms away by ca. 0.2 Å from the central 6*d* position. The scattering behavior in the current case has been approximately described by split positions at site with general multiplicity (48*l*). The 1/8 occupied Ba2 in this model is moved closer to the Ge framework (for instance Ge2 is now 3.78 Å away vs 4.02 Å if it were at the center); it also has a much-reduced value of B_{eq} for Ba2 (**Table 2**).

Table 3 lists selected interatomic distances in $Ba_8Li_5Ge_{41}$. To put the refined Ge–Ge and Li–Ge distances in broader context, we need to recall the covalent radius of the Ge atom (r_{Ge} ≈ 1.22 Å) [59] and the fact that in the average $Ba_8\square_3Ge_{43}$ structure, the Ge1 atoms at the 6*c* sites are surrounded by Ge3 atoms at 24*k* sites that are only 2.36 Å away (**Figure 3**). It is worth emphasizing this value is an average distance. The elongated atomic displacement ellipsoid of the Ge3 atoms indicates that these atoms respond to the local disorder by moving away when the site 6*c* is occupied by Li. Therefore, as the site 6*c* is mainly filled by Li atoms in $Ba_8Li_5Ge_{41}$, it is expected that distances between Li/Ge1 and Ge3 would be increased. Indeed, what is observed is that the Li/Ge1–Ge3 distances are ca. 2.51 Å from all refinements (**Table 3**). At the same time, there is no significant change in Ge2–Ge2 distances in comparison to those in the binary $Ba_8\square_3Ge_{43}$ clathrate.

Table 3. Selected interatomic distances (Å) of $Ba_8Li_x\square_{4-3x/4}Ge_{42-x/4}$ synthesized by *A*, *B* and *C* methods.

Atoms	Distances		
	A [a]	***B***	***C***
Ba1–Ge2 (×8)	3.4265(7)	3.4270(8)	3.4271(6)
Ba1–Ge3 (×12)	3.575(1)	3.5779(7)	3.5752(5)
Ba2–Li/Ge1 (×4)	3.619(4)	3.8201(2)	3.8218(2)
Ba2–Ge2 (×8)	3.782(4)	4.0198(5)	4.0196(5)
Ba2–Ge3 (×8)	3.490(3)	3.6181(5)	3.6207(4)
Ba2–Ge3 (×4)	4.028(5)	4.1956(8)	4.1965(8)
Li/Ge1–Ge3 (×4)	2.514(1)	2.5097(7)	2.5155(5)
Ge2–Ge2	2.507(1)	2.503(2)	2.5031(6)
Ge2–Ge3	2.513(1)	2.5130(5)	2.5127(4)
Ge3–Ge3	2.509(2)	2.514(1)	2.509(1)

[a] The refinement has Ba2 at site 48*l* that is 1/8 occupied. Not all possible Ba2–Ge distances are shown.

The $d_{Ba1–Ge2}$ and $d_{Ba1–Ge3}$ distances in the Ge_{20} cage range from 3.43 Å to 3.57 Å. These values are similar to the values for $d_{Ba2–Li/Ge1}$ and $d_{Ba2–Ge3}$ in the Ge_{24} cage when considering Ba2 off-center. If Ba2 is refined at site 6*d*, as done in the supplementary materials, the Ba1–Ge distances are shorter than the Ba2–Ge distances (**Table 3**). Of note is also the fact that Ba1–Ge distances in $Ba_8\square_3Ge_{43}$ (ranging from 3.39 Å to 3.64 Å) [7] are comparable with the Ba1–Ge distances in

$Ba_8Li_5Ge_{41}$, however, the Ba2–Ge distances in $Ba_8\square_3Ge_{43}$ (ranging from 3.53 Å to 4.10 Å) [7] are relatively shorter than the corresponding distances in $Ba_8Li_5Ge_{41}$.

A convenient way to systematically compare distances and lattice parameter in clathrate-I structures with substitutions and defects is to consider the normalized distances (*d*/*a*). To this point, our metrics from $Ba_8Li_5Ge_{41}$ can be compared with $Ba_8\square_3Ge_{43}$[7] with a large number of vacancies, $Ba_8Ni_{3.5}\square_{0.4}Ge_{42.1}$[35] having low number of vacancies and $Ba_8Pd_3Ge_{43}$ [43], $Ba_8Ga_{16}Ge_{30}$ [25] and $Ba_8Zn_8Ge_{38}$ [44] with reportedly no vacancies. The data are graphically presented in **Figure 5** and the exact values are tabulated in **Table 4**. The value of $d_{(6c–24k)}/a$ correlates remarkably well with the change in the cell parameter indicating that vacancies show a much stronger influence on the lattice parameter, than filler atoms' size. With decreasing number of vacancies, $d_{(6c–24k)}$ and $d_{(24k–24k)}$ become more equal. The decreasing value of $d_{(6c–24k)}/a$ ultimately reaches a plateau upon expansion of the unit cell beyond ca. 10.75 Å (**Table 4** and **Figure 5**). At the same time, there is no significant change in $d_{(16i–24k)}/a$, as expected. It is known that the high value of $d_{(6c–24k)}/a$ can be attributed to the presence of vacancies at 6*c* sites in binary clathrates [27,28,53]. When the 6*c* sites are filled by another atom, the value of $d_{(6c–24k)}/a$ decreases to a certain point and shows no further change, indicative of a saturation-like behavior. The normalized interatomic distances from our refinements fall well within this plateau confirming the notion that the Li incorporation into the structure leaves no vacancies in the Ge framework.

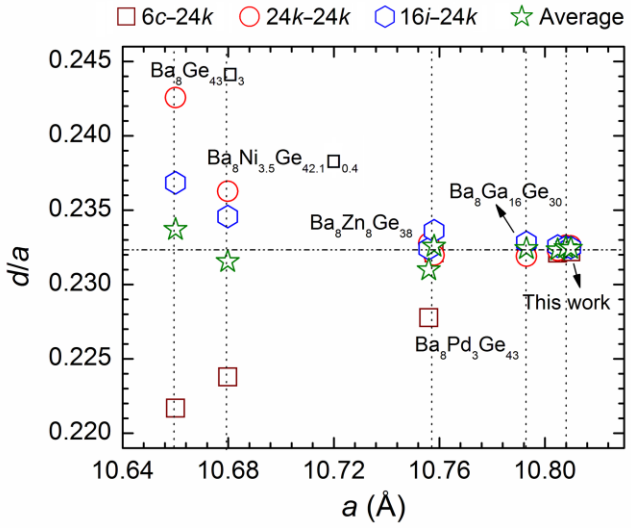

Figure 5. Normalized interatomic distances (*d*/*a*) with lattice parameter for selected clathrates-I.

The change in *d*/*a* is very well mapped in $K_8Li_xGe_{44–x/4}\square_{2–3x/4}$, where the varied Li incorporation has been studied in detail [53]. Correlating the number of vacancies per unit cell and the normalized $d_{(6c–24k)}/a$ value can be done with a linear regression as follows:

$$d(Ge1-Ge3)/a = 0.2336 - 0.0037 \times n_{\square}$$

The expression is empirically-derived and may capture best trends in cases with higher number of vacancies ($n_\square$) or having fewer substitutions. Given the similarities between the atomic sizes of K and Ba, the above regression can be a good approximation for the estimation of the number of vacancies in Ba/Ge-based clathrates too. For example, for $Ba_8\square_3Ge_{43}$, the calculated value of $n_\square$ from the above equation is of 3.2, which agrees very well with the structure refinements. Following the same equation, $n_\square$ for our samples can be estimated to be 0.35, 0.28 and 0.24 for *A*, *B* and *C*, respectively. On this note, and prior to discussing the electronic structure, we recall that for *x* = 5.33, $Ba_8Li_x\square_{4–3x/4}Ge_{42–x/4}$, i.e., for the limiting composition $Ba_8Li_{5.33}Ge_{40.67}$, the clathrate phase can be understood in terms of the Zintl-Klemm concept. Here, every termination (vacancy or Li substitution) of the Ge network (four-bonded Ge atoms, zero formal charge) will lead to four three-bonded Ge atoms with negative formal charges [28]. As such, the refined composition $Ba_8Li_{5.0}Ge_{41.0}$ is not expected to be fully balanced according to the following electron partition scheme: $[Ba^{2+}]_8[Li^+]_5[(3b\text{-}Ge^-)_4]_5[4b\text{-}Ge^0]_{16}(e^-)$. This agrees with the resistivity measurements for $Ba_8Li_5Ge_{41}$ single crystals (**Figure S4**), which show the sample to be a bad metal, not an intrinsic semiconductor (the expected behavior if it were to be considered as a Zintl phase). The binary $Ba_8Ge_{43}\square_3$ also exhibits metallicity since its composition can be rationalized as $[Ba^{2+}]_8[(3b\text{-}Ge^-)_4]_3[4b\text{-}Ge^0]_{21}(e^-)_4$. While the number of defects is very hard to control synthetically, the Li uptake can be varied with success. This has been previously demonstrated for the ternary clathrate $K_8Li_x\square_{2–3x/4}Ge_{44–x/4}$,[53] and the same tunability can be expected for $Ba_8Li_x\square_{4–3x/4}$, $Ge_{42–x/4}$. The reader is referred to the discussion in another article in a forthcoming issue of the journal.[76]

Table 4. Comparison of *d/a* values from the structural work on $Ba_8Li_x\square_{4-3x/4}Ge_{42-x/4}$ with some type-I clathrates. Letters *A*, *B*, and *C* refer to the three crystals from three different sample preparation techniques, as described in the experimental section. The small variation in the lattice constants are suggestive of slight compositional differences between the samples that cannot be accurately established on the basis of single-crystal X-ray diffraction methods.

Compound	*a* (Å)	*d*(6*c*–24*k*)/*a*	*d*(24*k*–24*k*)/*a*	*d*(16*i*–24*k*)/*a*	Average	Reference
$Ba_8Ge_{43}\square_3$	10.6565(2)	0.2217	0.2426	0.2368	0.2337	[28]
$Ba_8Ni_{3.5}Ge_{42.1}\square_{0.4}$	10.6798(2)	0.2238	0.2363	0.2346	0.2315	[35]
$Ba_8Pd_3Ge_{43}$	10.7560(2)	0.2278	0.2328	0.2324	0.2310	[43]
$Ba_8Zn_8Ge_{38}$	10.7580(1)	0.2321	0.2320	0.2336	0.2326	[44]
$Ba_8Ga_{16}Ge_{30}$	10.7930(6)	0.2325	0.2319	0.2328	0.2324	[25]
A	10.8079(9) [a]	0.2321	0.2323	0.2326	0.2323	This work
B	10.8048(11) [a]	0.2322	0.2326	0.2325	0.2325	This work
C	10.8098(11) [a]	0.2322	0.2326	0.2325	0.2324	This work

[a] Values from single-crystal X-ray diffraction work, carried out at 200 K.

Electronic structure and chemical bonding

While several binary clathrates of germanium—in particular with alkali metals as cations—reveal the electron-balanced situation by implementing of defects into the anionic framework, their ternary substitutional variants can reveal deviations from this trend [77]. Following this tendency, the Zintl balance for $Ba_8Li_5Ge_{41}$ as mentioned earlier, is $[Ba^{2+}]_8[(4b\text{-}Li^{3-}]_5(4b\text{-}Ge^0]_{41}(1e^-)$, and essentially reveals a small amount of excess electrons. The expected "electron-richness" was first confirmed for the optimized ordered model $Ba_8Li_6Ge_{40}$ (*a* = 10.7126 Å, *x*(Ge2) = 0.1827, *x*(Ge3) = 0.1153, *y*(Ge3) = 0.3118).[78]

Following the Zintl scheme $[Ba^{2+}]_8[(4b\text{-}Li^{3-}]_6(4b\text{-}Ge^0]_{40}(3h^+)$ and being in close analogy with the previous results,[78] the electronic density of states for $Ba_8Li_6Ge_{40}$, calculated with experimental parameters for $Ba_8Li_5Ge_{41}$ and full Li-occupancy of the 6*c* site (**Figure 6**, bottom) contains three large regions below the Fermi level, dominated by the *s*- and *p*- states of germanium together with the *s*-states of lithium and the contributions of *s*-states of Ba distributed over the whole energy range, with a gap of ca 0.08 eV and not fully occupied 'bonding' states below the gap.

Implementation of the Li/Ge disorder for the composition $Ba_8Li_5Ge_{41}$ (**Figure 6**, top, cf. **Electronic structure calculations** above) preserves the basic three-region construction of the DOS. Also, the contributions of the atomic states to different regions are similar. The first difference agrees with the electron-counting scheme above: the Fermi level is moved to the 'anti-bonding' states (the Zintl-optimal Li content is *x* = 5⅓). More interesting is the fact, that the gap, obtained in the ordered model $Ba_8Li_6Ge_{40}$, is now closed (< 0.01 eV). This correlates well with the experimentally found temperature dependence of the electronic transport revealing bad-metal behavior (Figure S4)).

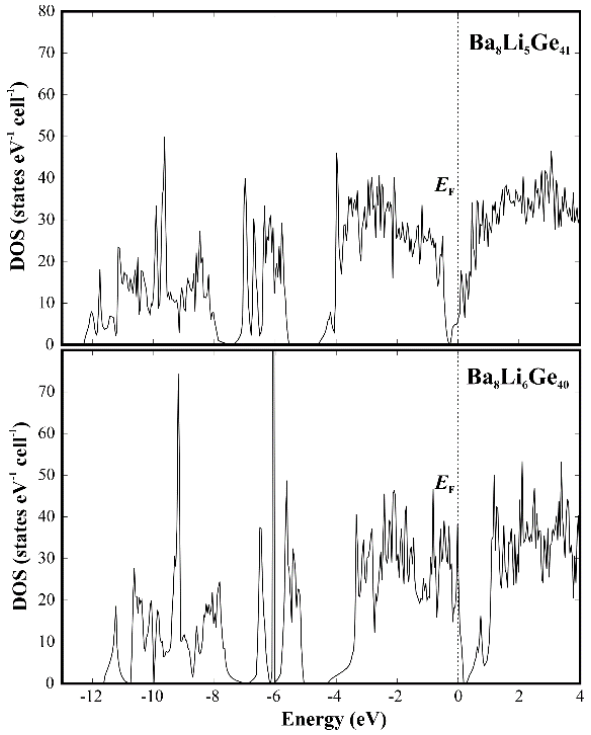

Figure 6. Calculated total electronic density of states (DOS)) for $Ba_8Li_5Ge_{41}$ (top) in comparison with $Ba_8Li_6Ge_{40}$ (bottom).

The tiny differences in the electronic DOS between $Ba_8Li_5Ge_{41}$ and $Ba_8Li_6Ge_{40}$ are also represented in atomic interactions studied by position space approach.[68,79] Analysis of the effective QTAIM charges in $Ba_8Li_5Ge_{41}$ obtained applying the QTAIM approach on electron density (**Figure 7**, top) shows only small deviations from the values reported earlier for the fully substituted model $Ba_8Li_6Ge_{40}$ [78] : +1.20 to +1.25 for Ba1 in $Ba_8Li_5Ge_{41}$ (+1.2 in $Ba_8Li_6Ge_{40}$),+1.25 to +1.30 for Ba2 (+1.3), +0.79 for Li (+0.80), -0.5 for Ge1, –0.4 to –0.5 for Ge2 (–0.4), –0.3 to –0.5 for Ge3 (–0.4). Worth noticing is that the charge of Ge3 atoms, which are in contact with Li (Li1+2Ge2+Ge3, –0.3 to –0.35) does not differ essentially from Ge3 coordinated only by Ge (Ge1+2Ge2+Ge3, –0.35).

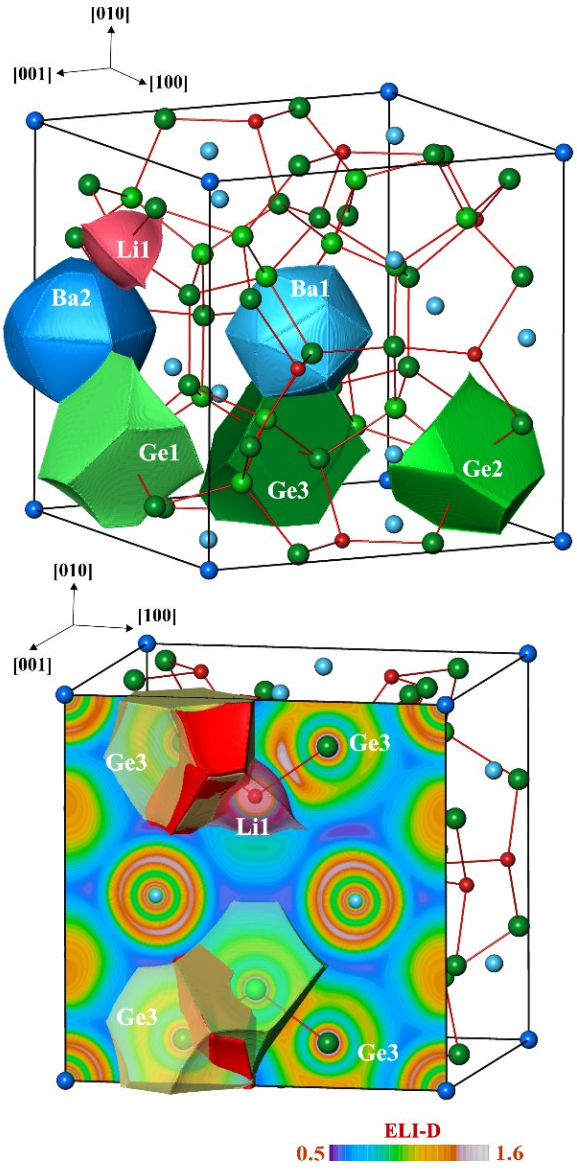

Figure 7. Chemical bonding in $Ba_8Li_5Ge_{41}$: (top) Characteristic shapes and effective charges of the QTAIM atoms. (bottom) Polarity of Li1–Ge3 and Ge1–Ge3 bonds revealed from the distribution of ELI-D in the (001) plane and bond basins for Li1–Ge3 (red shape, top) and Ge1–Ge3 (red shape, bottom) bonds in relation to the atomic basins of Li1, Ge1 and Ge3 species (transparent shapes).

From the QTAIM analysis of electron density, Ba is playing a role of a cation in the barium-lithium clathrate investigated. The role of lithium can be understood from the combined analysis of electron localizability indicator and electron density, applying the intersection technique. Calculations performed on the ordered $Ba_8Li_5Ge_{41}$ model allow studying separately bonding peculiarities of different atoms at the 6*c* position (**Figure 7**, bottom). While the QTAIM shapes of Ge1 and Ge3 atoms involved into Ge1–Ge3 bonds show flat common faces (yellow transparent shapes in the bottom part of the bottom panel in **Figure 7**), the common surface for Li1 and Ge3 QTAIM atoms is convex toward germanium nucleus. Such behavior was recently observed for $Mg_{3-x}Ga_{1+x}Ir$ [80] and $Mg_{29-x}Pt_{5+y}$ [81] and is characteristic feature of polar bonding in position space representation. This is clearly confirmed studying the participation of Ge and Li in the ELI-D bonds basins (red shapes, **Figure 7** bottom panel). While the Ge1–Ge3 bond basin is split equally between the according QTAIM shapes, Ge3 is contributing more than 90% of the bond population of the Li1-Ge3 bond basin. This is the clear sign of the strongly polar covalent character of this interaction, which is confirmed by the presence of the separated ELI-D maximum for this bond (cf. ELI-D distribution map in the (001) plane, **Figure 7** bottom). For the comparison, the fully ionic interaction between Ba and the anionic framework does not show separated maximum in the ELI-D distribution.

Conclusions

The family of ternary clathrates with substitution of late transition metals and group 13 metals have been widely studied before [3,8,11,27,28,30–32,48]. Clathrates with lithium substitutions, however, have scarcely been explored in detail. The $Ba_8Li_5Ge_{41}$ clathrate, which is the subject of this paper, adds a great deal of new knowledge in this field. Crystals with the composition $Ba_8Li_5Ge_{41}$ were successfully synthesized by different methods. The crystal structure was elucidated based on single-crystal X-ray diffraction data. The observation of Li substitution on Ge sites becomes an experimental validation of the notion that such behavior would be favorable in Ba/Ge-clathrates, as established by DFT calculations before. This is confirmed by electronic structure calculations and analysis of chemical bonding applying the electron density/ electron localizability approach. While the barium interaction with the Li-Ge framework is ionic, the lithium-germanium bonds are strongly polar covalent.

$Ba_8Li_5Ge_{41}$ is the second only ternary clathrate with the type-I crystal structure, after $K_8Li_xGe_{44-x/4}\square_{2-3x/4}$,[28] where such phenomenology is observed. There also exist precedents for Li substitution on Ge sites in type-II clathrates,[63] and Na substitution on Sn sites in type-III clathrates,[62] which suggests that the clathrates might be generally amenable to similar alterations within their structures. In this context, future research to synthesize more clathrate compounds with alkali or alkaline-earth metal atoms within the framework can be suggested.

Author Contributions

Kowsik Ghosh: Conceptualization, Investigation, Methodology, Formal analysis, Visualization, Writing - original draft.

Alexander Ovchinnikov: Conceptualization, Investigation, Formal analysis, Writing - review & editing.

Michael Baitinger: Investigation, Formal analysis, Writing - review & editing.

Mitja Krnel: Resistivity measurements, Writing - review & editing.

Ulrich Burkhardt: WDX measurements, Writing - review & editing.

Yuri Grin: Electronic structure calculations, Formal analysis, Chemical bonding analysis, Writing - review & editing.

Svilen Bobev: Conceptualization, Supervision, Project administration, Writing - review & editing.

Conflicts of interest

There are no conflicts to declare.

Acknowledgements

This work was supported by the National Science Foundation through grant DMR-2004579.

Notes and references

1 Kasper, J. S.; Hagenmuller, P.; Pouchard, M.; Cros, C. Clathrate Structure of Silicon Na_8Si_{36} and Na_xSi_{136} (x < 11). *Science (80-.).* **1965**, *150* (3704), 1713–1714. https://doi.org/10.1126/science.150.3704.1713.

2 Bobev, S.; Sevov, S. C. Clathrates of Group 14 with Alkali Metals: An Exploration. *J. Solid State Chem.* **2000**, *153* (1), 92–105. https://doi.org/10.1006/jssc.2000.8755.

3 Bryan, J. D.; Srdanov, V. I.; Stucky, G. D. Superconductivity in Germanium Clathrate $Ba_8Ga_{16}Ge_{30}$. *Phys. Rev. B* **1999**, *60* (5), 3064–3067. https://doi.org/10.1103/PhysRevB.60.3064.

4 Kawaji, H.; Horie, H.; Yamanaka, S.; Ishikawa, M. Superconductivity in the Silicon Clathrate Compound $(Na,Ba)_8Si_{46}$. *Phys. Rev. Lett.* **1995**, *74* (8), 1427–1429. https://doi.org/10.1103/PhysRevLett.74.1427.

5 Reny, E.; San-Miguel, A.; Guyot, Y.; Masenelli, B.; Mélinon, P.; Saviot, L.; Yamanaka, S.; Champagnon, B.; Cros, C.; Pouchard, M.; Borowski, M.; Dianoux, A. J. Vibrational Modes in Silicon Clathrate Compounds: A Key to Understanding Superconductivity. *Phys. Rev. B - Condens. Matter Mater. Phys.* **2002**, *66* (1), 1–7. https://doi.org/10.1103/PhysRevB.66.014532.

6 Connétable, D.; Timoshevskii, V.; Masenelli, B.; Beille, J.; Marcus, J.; Barbara, B.; Saitta, A. M.; Rignanese, G. M.; Mélinon, P.; Yamanaka, S.; Blase, X. Superconductivity in Doped sp^3 Semiconductors: The Case of the Clathrates. *Phys. Rev. Lett.* **2003**, *91* (24), 1–4. https://doi.org/10.1103/PhysRevLett.91.247001.

7 Fukuoka, H.; Kiyoto, J.; Yamanaka, S. Superconductivity and Crystal Structure of the Solid Solutions of $Ba_{8-\delta}Si_{46-x}Ge_x$ ($0 \le x \le 23$) with Type I Clathrate Structure. *J. Solid State Chem.* **2003**, *175* (2), 237–244. https://doi.org/10.1016/S0022-4596(03)00253-6.

8 Condron, C. L.; Kauzlarich, S. M.; Gascoin, F.; Snyder, G. J. Thermoelectric Properties and Microstructure of $Ba_8Al_{14}Si_{31}$ and $EuBa_7Al_{13}Si_{33}$. *Chem. Mater.* **2006**, *18* (20), 4939–4945. https://doi.org/10.1021/cm061483u.

9 Condron, C. L.; Kauzlarich, S. M.; Nolas, G. S. Structure and Thermoelectric Characterization of $A_xBa_{8-x}Al_{14}Si_{31}$ (A = Sr, Eu) Single Crystals. *Inorg. Chem.* **2007**, *46* (7), 2556–2562. https://doi.org/10.1021/ic062115v.

10 Zhang, H.; Borrmann, H.; Oeschler, N.; Candolfi, C.; Schnelle, W.; Schmidt, M.; Burkhardt, U.; Baitinger, M.; Zhao, J. T.; Grin, Y. Atomic Interactions in the P-Type Clathrate I $Ba_8Au_{5.3}Ge_{40.7}$. *Inorg. Chem.* **2011**, *50* (4), 1250–1257. https://doi.org/10.1021/ic1016559.

11 Blake, N. P.; Møllnitz, L.; Kresse, G.; Metiu, H. Why Clathrates Are Good Thermoelectrics: A Theoretical Study of $Sr_8Ga_{16}Ge_{30}$. *J. Chem. Phys.* **1999**, *111* (7), 3133–3144. https://doi.org/10.1063/1.479615.

12 Tsujii, N.; Roudebush, J. H.; Zevalkink, A.; Cox-Uvarov, C. A.; Snyder, G. J.; Kauzlarich, S. M. Phase Stability and Chemical Composition Dependence of the Thermoelectric Properties of the Type-I Clathrate $Ba_8Al_xSi_{46-x}$ ($8 \le x \le 15$). *J. Solid State Chem.* **2011**, *184* (5), 1293–1303. https://doi.org/10.1016/j.jssc.2011.03.038.

13 Saramat, A.; Svensson, G.; Palmqvist, A. E. C.; Stiewe, C.; Mueller, E.; Platzek, D.; Williams, S. G. K.; Rowe, D. M.; Bryan, J. D.; Stucky, G. D. Large Thermoelectric Figure of Merit at High Temperature in Czochralski-Grown Clathrate $Ba_8Ga_{16}Ge_{30}$. *J. Appl. Phys.* **2006**, *99* (2). https://doi.org/10.1063/1.2163979.

14 Nolas, G. S.; Slack, G. A.; Schujman, S. B. Chapter 6: Semiconductor Clathrates: A Phonon Glass Electron Crystal Material with Potential for Thermoelectric Applications; 2001; Vol. 69. https://doi.org/10.1016/S0080-8784(01)80152-6.

15 Uemura, T.; Akai, K.; Koga, K.; Tanaka, T.; Kurisu, H.; Yamamoto, S.; Kishimoto, K.; Koyanagi, T.; Matsuura, M. Electronic Structure and Thermoelectric Properties of Clathrate Compounds $Ba_8Al_xGe_{46-x}$. *J. Appl. Phys.* **2008**, *104* (1). https://doi.org/10.1063/1.2947593.

16 Kawaguchi, T.; Tanigaki, K.; Yasukawa, M. Ferromagnetism in Germanium Clathrate: $Ba_8Mn_2Ge_{44}$. *Appl. Phys. Lett.* **2000**, *77* (21), 3438–3440. https://doi.org/10.1063/1.1328048.

17 Mott, N. F. Properties of Compounds of Type Na_xSi_{46} and Na_xSi_{136}. *J. Solid State Chem.* **1973**, *6* (3), 348–351. https://doi.org/10.1016/0022-4596(73)90221-1.

18 Yang, J.; Tse, J. S. Silicon Clathrates as Anode Materials for Lithium Ion Batteries? *J. Mater. Chem. A* **2013**, *1* (26), 7782–7789. https://doi.org/10.1039/c3ta11050h.

19 Warrier, P.; Koh, C. A. Silicon Clathrates for Lithium Ion Batteries: A Perspective. *Appl. Phys. Rev.* **2016**, *3* (4). https://doi.org/10.1063/1.4958711.

20 Peng, X.; Wei, Q.; Li, Y.; Chan, C. K. First-Principles Study of Lithiation of Type I Ba-Doped Silicon Clathrates. *J. Phys. Chem. C* **2015**, *119* (51), 28247–28257. https://doi.org/10.1021/acs.jpcc.5b07523.

21 Li, Y.; Raghavan, R.; Wagner, N. A.; Davidowski, S. K.; Baggetto, L.; Zhao, R.; Cheng, Q.; Yarger, J. L.; Veith, G. M.; Ellis-Terrell, C.; Miller, M. A.; Chan, K. S.; Chan, C. K. Type I Clathrates as Novel Silicon Anodes: An Electrochemical and Structural Investigation. *Adv. Sci.* **2015**, *2* (6), 1–12. https://doi.org/10.1002/advs.201500057.

22 Chan, K. S.; Miller, M. A.; Liang, W.; Ellis-Terrell, C.; Chan, C. K. First Principles and Experimental Studies of Empty Si_{46} as

Anode Materials for Li-Ion Batteries. *J. Mater. Res.* **2016**, *31* (23), 3657–3665. https://doi.org/10.1557/jmr.2016.408.

23 Karttunen, A. J.; Fässler, T. F.; Linnolahti, M.; Pakkanen, T. A. Structural Principles of Semiconducting Group 14 Clathrate Frameworks. *Inorg. Chem.* **2011**, *50* (5), 1733–1742. https://doi.org/10.1021/ic102178d.

24 Dubois, F.; Fässler, T. F. Ordering of Vacancies in Type-I Tin Clathrate: Superstructure of $Rb_8Sn_{44}\square_2$. *J. Am. Chem. Soc.* **2005**, *127* (10), 3264–3265. https://doi.org/10.1021/ja043500r.

25 Blake, N. P.; Bryan, D.; Latturner, S.; Møllnitz, L.; Stucky, G. D.; Metiu, H. Structure and Stability of the Clathrates $Ba_8Ga_{16}Ge_{30}$, $Sr_8Ga_{16}Ge_{30}$, $Ba_8Ga_{16}Si_{30}$, and $Ba_8In_{16}Sn_{30}$. *J. Chem. Phys.* **2001**, *114* (22), 10063–10074. https://doi.org/10.1063/1.1370949.

26 von Schnering, H.-G.; Kröner, R.; Baitinger, M.; Peters, K.; Nesper, R.; Grin, Y. Crystal Structure of the Defect Clathrate $Cs_8Sn_{44}\square_2$. *Z. Krist. - New Cryst. Struct.* **2000**, *215* (2), 205–206. https://doi.org/10.1515/ncrs-2000-0207.

27 von Schnering, H.-G.; Llanos, J.; Peters, K.; Baitinger, M.; Grin, Y.; Nesper, R. Refinement of the Crystal Structure of $K_8Ge_{44}\square_2$, an Intermetallic Clathrate I. *Z. Krist. - New Cryst. Struct.* **2011**, *226* (1), 9–10. https://doi.org/10.1524/ncrs.2011.0005.

28 Carrillo-Cabrera, W.; Curda, J.; Peters, K.; Paschen, S.; Baenitz, M.; Grin, Y.; von Schnering, H.-G. Crystal Structure of the Defect Clathrate-I, Ba_8Ge_{43}. Z. Krist. **2000**, *215*, 321–322. https://doi.org/10.1515/ncrs-2000-0207.

29 Møllnitz, L.; Blake, N. P.; Meitu, H. Effects of Morphology on the Electronic and Transport Properties of Sn-Based Clathrates. *J. Chem. Phys.* **2002**, *117* (3), 1302–1312. https://doi.org/10.1063/1.1485728.

30 Sui, F.; Kauzlarich, S. M. Tuning Thermoelectric Properties of Type I Clathrate $K_{8-x}Ba_xAl_{8+x}Si_{39-x}$ through Barium Substitution. *Chem. Mater.* **2016**, *28* (9), 3099–3107. https://doi.org/10.1021/acs.chemmater.6b00566.

31 Sui, F.; He, H.; Bobev, S.; Zhao, J.; Osterloh, F. E.; Kauzlarich, S. M. Synthesis, Structure, Thermoelectric Properties, and Band Gaps of Alkali Metal Containing Type I Clathrates: $A_8Ga_8Si_{38}$ (*A* = K, Rb, Cs) and $K_8Al_8Si_{38}$. *Chem. Mater.* **2015**, *27* (8), 2812–2820. https://doi.org/10.1021/cm504436v.

32 Christensen, M.; Lock, N.; Overgaard, J.; Iversen, B. B. Crystal Structures of Thermoelectric n- and p-Type $Ba_8Ga_{16}Ge_{30}$ Studied by Single Crystal, Multi-temperature, Neutron Diffraction, Conventional X-Ray Diffraction and Resonant Synchrotron X-Ray Diffraction. *J. Am. Chem. Soc.* **2006**, *128* (49), 15657–15665. https://doi.org/10.1021/ja063695y.

33 Dopilka, A.; Zhao, R.; Weller, J. M.; Bobev, S.; Peng, X.; Chan, C. K. Experimental and Computational Study of the Lithiation of $Ba_8Al_yGe_{46-y}$ Based Type I Germanium Clathrates. *ACS Appl. Mater. Interfaces* **2018**, *10* (44), 37981–37993. https://doi.org/10.1021/acsami.8b11509.

34 Chakoumakos, B. C.; Sales, B. C.; Mandrus, D. G. Structural Disorder and Magnetism of the Semiconducting Clathrate $Eu_8Ga_{16}Ge_{30}$. *J. Alloys Compd.* **2001**, *322* (1–2), 127–134. https://doi.org/10.1016/S0925-8388(01)01169-0.

35 Nguyen, L. T. K.; Aydemir, U.; Baitinger, M.; Bauer, E.; Borrmann, H.; Burkhardt, U.; Custers, J.; Haghighirad, A.; H¨ofler, R.; Luther, K. D.; Ritter, F.; Assmus, W.; Grin, Y.; Paschen, S. Atomic Ordering and Thermoelectric Properties of the N-Type Clathrate $Ba_8Ni_{3.5}Ge_{42.1}$. *Dalt. Trans.* **2010**, *39*, 1071–1077. https://doi.org/10.1039/b916400f.

36 Johnsen, S.; Bentien, A.; Madsen, G. K. H.; Iversen, B. B.; Nygren, M. Crystal Structure, Band Structure, and Physical Properties of $Ba_8Cu_{6-x}Ge_{40+x}$ (0< x <0.7). *Chem. Mater.* **1006**, *18*, 4633–4642. https://doi.org/10.1016/j.intermet.2017.02.009.

37 Johnsen, S.; Bentien, A.; Madsen, G. K. H.; Nygren, M.; Iversen, B. B. Crystal Structure and Transport Properties of Nickel Containing Germanium Clathrates. *Phys. Rev. B - Condens. Matter Mater. Phys.* **2007**, *76* (24), 1–9. https://doi.org/10.1103/PhysRevB.76.245126.

38 Christensen, M.; Johnsen, S.; Iversen, B. B. Thermoelectric Clathrates of Type I. *Dalt. Trans.* **2010**, *39* (4), 978–992. https://doi.org/10.1039/b916400f.

39 Xu, J.; Wu, J.; Shao, H.; Heguri, S.; Tanabe, Y.; Liu, Y.; Liu, G. Q.; Jiang, J.; Jiang, H.; Tanigaki, K. Structure and Thermoelectric Properties of the n-Type Clathrate $Ba_8Cu_{5.1}Ge_{40.2}Sn_{0.7}$. *J. Mater. Chem. A* **2015**, *3* (37), 19100–19106. https://doi.org/10.1039/c5ta04168f.

40 Slack, G. New Materials and Performance Limits for Thermoelectric Cooling. *CRC Handb. Thermoelectr.* **1995**. https://doi.org/10.1201/9781420049718.ch34.

41 Zeiringer, I.; Melnychenko-Koblyuk, N.; Grytsiv, A.; Bauer, E.; Giester, G.; Rogl, P. Phase Equilibria, Crystal Chemistry and Physical Properties of Au-Ba-Ge Clathrates. *J. Phase Equilibria Diffus.* **2011**, *32* (2), 115–127. https://doi.org/10.1007/s11669-011-9852-7.

42 Melnychenko-Koblyuk, N.; Grytsiv, A.; Berger, S.; Kaldarar, H.; Michor, H.; Röhrbacher, F.; Royanian, E.; Bauer, E.; Rogl, P.; Schmid, H.; Giester, G. Ternary Clathrates Ba-Cd-Ge: Phase Equilibria, Crystal Chemistry and Physical Properties. *J. Phys. Condens. Matter* **2007**, *19* (4). https://doi.org/10.1088/0953-8984/19/4/046203.

43 Melnychenko-Koblyuk, N.; Grytsiv, A.; Rogl, P.; Rotter, M.; Bauer, E.; Durand, G.; Kaldarar, H.; Lackner, R.; Michor, H.; Royanian, E.; Koza, M.; Giester, G. Clathrate Formation in the Ba-Pd-Ge System: Phase Equilibria, Crystal Structure, and Physical Properties. *Phys. Rev. B - Condens. Matter Mater. Phys.* **2007**, *76* (14), 1–11. https://doi.org/10.1103/PhysRevB.76.144118.

44 Melnychenko-Koblyuk, N.; Grytsiv, A.; Fornasari, L.; Kaldarar, H.; Michor, H.; Röhrbacher, F.; Koza, M.; Royanian, E.; Bauer, E.; Rogl, P.; Rotter, M.; Schmid, H.; Marabelli, F.; Devishvili, A.; Doerr, M.; Giester, G. Ternary Clathrates Ba-Zn-Ge: Phase Equilibria, Crystal Chemistry and Physical Properties. *J. Phys. Condens. Matter* **2007**, *19* (21). https://doi.org/10.1088/0953-8984/19/21/216223.

45 Melnychenko-Koblyuk, N.; Grytsiv, A.; Rogl, P.; Rotter, M.; Lackner, R.; Bauer, E.; Fornasari, L.; Marabelli, F.; Giester, G. Structure and Physical Properties of Type-I Clathrate Solid-Solution $Ba_8Pt_xGe_{46-x-y}$ (y = Vacancy). *Phys. Rev. B - Condens. Matter Mater. Phys.* **2007**, *76* (19), 1–7. https://doi.org/10.1103/PhysRevB.76.195124.

46 Aydemir, U.; Candolfi, C.; Borrmann, H.; Baitinger, M.; Ormeci, A.; Carrillo-Cabrera, W.; Chubilleau, C.; Lenoir, B.; Dauscher, A.; Oeschler, N.; Steglich, F.; Grin, Y. Crystal Structure and Transport Properties of $Ba_8Ge_{43}\square_3$. *Dalt. Trans.* **2010**, *39*, 1078–1088. https://doi.org/10.1039/b916400f.

47 Candolfi, C.; Ormeci, A.; Aydemir, U.; Baitinger, M.; Oeschler, N.; Grin, Y.; Steglich, F. Multiband Conduction in the Type-I Clathrate $Ba_8Ge_{43}\square_3$. *Phys. Rev. B - Condens. Matter Mater. Phys.* **2011**, *84* (20), 1–8. https://doi.org/10.1103/PhysRevB.84.205118.

48 Carrillo-Cabrera, W.; Budnyk, S.; Prots, Y.; Grin, Y. Ba_8Ge_{43} Revisited: a $2a_0 \times 2a_0 \times 2a_0$ Superstructure of the Clathrate-I Type with Full Vacancy Ordering. *Z. Anorg. Allg. Chem.* **2004**, *630* (13–14), 2267–2276. https://doi.org/10.1002/zaac.200400268.

49 Liang, Y.; Carrillo-Cabrera, W.; Ormeci, A.; Böhme, B.; Baitinger, M.; Grin, Y. The 2×2×2 Superstructure in the Clathrate-I $K_8Li_xGe_{44-x/4}\square_{2-3x/4}$. *Z. Anorg. Allg. Chem.* **2015**, *641* (2), 339–347. https://doi.org/10.1002/zaac.201400565.

50 Zeiringer, I.; Chen, M.; Bednar, I.; Royanian, E.; Bauer, E.; Podloucky, R.; Grytsiv, A.; Rogl, P.; Effenberger, H. Phase

Equilibria, Crystal Chemistry, Electronic Structure and Physical Properties of Ag-Ba-Ge Clathrates. *Acta Mater.* **2011**, *59* (6), 2368–2384. https://doi.org/10.1016/j.actamat.2010.12.033.

51 Wunderlich, W.; Amano, M.; Matsumura, Y. Electronic Band-Structure Calculations of $Ba_8Me_xSi_{46-x}$ Clathrates with Me = Mg, Pd, Ni, Au, Ag, Cu, Zn, Al, Sn. *J. Electron. Mater.* **2014**, *43* (6), 1527–1532. https://doi.org/10.1007/s11664-013-2770-1.

52 Baitinger, M.; Nguyen, H. D.; Candolfi, C.; Antonyshyn, I.; Meier-Kirchner, K.; Veremchuk, I.; Razinkov, V.; Havryluk, M.; Cardoso-Gil, R.; Burkhardt, U.; Böhme, B.; Anatychuk, L.; Grin, Y. Thermoelectric Characterization of the Clathrate-I Solid Solution $Ba_{8-\delta}Au_xGe_{46-x}$. *Appl. Phys. Lett.* **2021**, *119* (6). https://doi.org/10.1063/5.0059166.

53 Liang, Y.; Böhme, B.; Ormeci, A.; Borrmann, H.; Pecher, O.; Haarmann, F.; Schnelle, W.; Baitinger, M.; Grin, Y. A Clathrate-I Phase with Li-Ge Framework. *Chem. - A Eur. J.* **2012**, *18* (32), 9818–9822. https://doi.org/10.1002/chem.201202069.

54 Dopilka, A.; Childs, A.; Bobev, S.; Chan, C. K. Understanding the Amorphous Lithiation Pathway of the Type I Ba_8Ge_{43} Clathrate with Synchrotron X-Ray Characterization. *Chem. Mater.* **2020**, *32* (21), 9444–9457. https://doi.org/10.1021/acs.chemmater.0c03641.

55 Sheldrick, G. M. SHELXT - Integrated Space-Group and Crystal-Structure Determination. *Acta Crystallogr. Sect. A Found. Crystallogr.* **2015**, *71* (1), 3–8. https://doi.org/10.1107/S2053273314026370.

56 Sheldrick, G. M. Crystal Structure Refinement with SHELXL. *Acta Crystallogr. Sect. C Struct. Chem.* **2015**, *71*, 3–8. https://doi.org/10.1107/S2053229614024218.

57 Akselrud, L. G.; Zavalii, P. Y.; Grin, Y. N.; Pecharski, V. K.; Baumgartner, B.; Wölfel, E. Use of the CSD Program Package for Structure Determination from Powder Data. *Mater. Sci. Forum* **1993**, *133–136*, 335–342. https://doi.org/10.4028/www.scientific.net/msf.133-136.335.

58 Rajput, K.; Baranets, S.; Bobev, S. Observation of an Unexpected N-Type Semiconducting Behavior in the New Ternary Zintl Phase Eu_3InAs_3. *Chem. Mater.* **2020**, *32* (22), 9616–9626. https://doi.org/10.1021/acs.chemmater.0c03168.

59 Pauling, L. The Nature of the Chemical Bonding, 3rd Ed. *Cornell Univ. Press Ithaca, NY, USA* **1960**, 403. https://doi.org/10.1002/jps.3030300111.

60 Schäfer, M. C.; Bobev, S. Synthesis and Structural Characterization of the New Clathrates $K_8Cd_4Ge_{42}$, $Rb_8Cd_4Ge_{42}$, and $Cs_8Cd_4Ge_{42}$. *Materials (Basel).* **2016**, *9* (4). https://doi.org/10.3390/ma9040236.

61 Nesper, R. The Zintl-Klemm Concept - A Historical Survey. *Z. Anorg. Allg. Chem.* **2014**, *640* (14), 2639–2648. https://doi.org/10.1002/zaac.201400403.

62 Bobev, S.; Sevov, S. C. Clathrate III of Group 14 Exists after All. *J. Am. Chem. Soc.* **2001**, *123* (14), 3389–3390. https://doi.org/10.1021/ja010010f.

63 Böhme, B.; Wei, K.; Bobnar, M.; Prots, Y.; Burkhardt, U.; Baitinger, M.; Nolas, G. S.; Grin, Y. A Type-II Clathrate with a Li-Ge Framework. *Z. Krist. - Cryst. Mater.* **2017**, *232* (7–9), 543–556. https://doi.org/10.1515/zkri-2017-2046.

64 P.-F. Lory, S. Pailhès, V. M. Giordano, H. Euchner, H. D. Nguyen, R. Ramlau, H. Borrmann, M. Schmidt, M. Baitinger, M. Ikeda, P. Tomeš, M. Mihalkovi, C. Allio, M. R. Johnson, H. Schober, Y. Sidis, F. Bourdarot, L. P. Regnault, J. Ollivier, S. Paschen, Yu. Grin, M. de Boissieu, Direct measurement of individual phonon lifetimes in the clathrate compound $Ba_{7.81}Ge_{40.67}Au_{5.33}$. *Nature Comm*. **2017**, *491*, 1–10.

65 K. Koepernik, H. Eschrig, Full-potential nonorthogonal local-orbital minimum-basis band-structure scheme. *Phys. Rev. B* **1999**, *59*, 1743–1757.

66 J. P. Perdew, Y. Wang, Accurate and simple analytic representation of the electron-gas correlation energy. *Phys. Rev. B* **1992**, *45*, 13244–13249.

67 M. Kohout, Bonding indicators from electron pair density functionals. *Faraday Discussions* **2007**, *135*, 43-54.

68 F. R. Wagner, V. Bezugly, M. Kohout, Yu. Grin, Charge decomposition analysis of the Electron Localizability Indicator: A Bridge between the Orbital and Direct Space Representation of the Chemical Bond. *Chem. Eur. J.* **2007**, *13*, 5724–5741.

69 M. Kohout, F. Wagner, Yu. Grin, Atomic Shells From the Electron Localizability in Momentum Space. *Int. J. Quantum Chem.* **2006**, *106*, 1499–1507.

70 A. Ormeci, H. Rosner, F. Wagner, M. Kohout, Yu. Grin, Electron localization function in full-potential representation for crystalline materials. *J. Phys. Chem. A* **2006**, *110*, 1100–1105.

71 M. Kohout, DGrid, versions 4.6-5.0, Dresden, **2018-2021**.

72 R. F. W. Bader, *Atoms in molecules: A Quantum Theory Oxford University*, **1990**.

73 S. Raub, G. Jansen, A quantitative measure of bond polarity from the electron localization function and the theory of atoms in molecules. *Theor. Chem. Acc.* **2001**, *106*, 223-232.

74 D. Bende, F. R. Wagner, Yu. Grin, 8 − N Rule and Chemical Bonding in Main-Group MgAgAs Type Compounds. *Inorg. Chem.* **2015**, *54*, 3970–3978.

75 F. Wagner, D. Bende, Yu. Grin, Heteropolar bonding and a position-space representation of the 8–N rule. *Dalton Trans.* **2016**, *45*, 3236–3243.

76 Liang et al, *Dalton Trans.* **2023**, *in preparation*

77 M. Baitinger, B. Böhme, A. Ormeci, Yu. Grin. Solid State Chemistry of Clathrate Phases: Crystal Structure, Chemical Bonding and Preparation Routes. In: The Physics and Chemistry of Inorganic Clathrates, Springer, 2014, p. 35-–64.

78 A. Ormeci, Yu. Grin, Coexistence of ionic and covalent atomic interactions (bonding inhomogeneity) and thermoelectric properties of intermetallic clathrates. Journal of Thermoelectricity № 6, **2015**, 16–32.

79 F. R. Wagner, Yu. Grin, Chemical bonding analysis in position space. In: Comprehensive Inorganic Chemistry III. Elsevier, 2022, https://doi.org/10.1016/B978-0-12-823144-9.00189-8.

80 O. Sichevych, Y. Prots, W. Schnelle, F. R. Wagner, Y. Grin, Polycation–Polyanion Architecture of the Intermetallic Compound $Mg_{3-x}Ga_{1+x}Ir$, *Molecules* **2022**, *27*, 659.

81 L. Agnarelli, Y. Prots, R. Ramlau, M. Schmidt, U. Burkhardt, A. Leithe-Jasper, Y. Grin, $Mg_{29-x}Pt_{4+y}$: Chemical Bonding Inhomogeneity and Structural Complexity. *Inorg. Chem*. **2022**, *61*, 16148–16155.